CAV2009 – Paper No. 122

Simulation of Cavitation Instabilities in Inducers

Ashvin Hosangadi
Combustion Research and Flow Technology, Inc.
(CRAFT Tech)
Pipersville, PA 18947

Vineet Ahuja
Combustion Research and Flow Technology, Inc.
(CRAFT Tech)
Pipersville, PA 18947

Ronald J. Ungewitter
Combustion Research and Flow Technology, Inc. (CRAFT Tech)
Pipersville, PA 18947

ABSTRACT

The cavitating performance of a sub-scale configuration of the SSME low pressure fuel pump (LPFP) has been simulated at off-design flow conditions where a back-flow vortex is generated at the leading edge. The numerical simulations have been compared with measured experimental data both for velocity profiles upstream of the inducer as well dynamic pressure traces on the shroud at the leading edge. Velocity profiles in the back-flow vortex for flow rates down to 70 percent of design were quantified; the swirl velocity comparisons were good while the axial velocity profile were reasonable but slightly over predicted the core velocity.

Dynamic cavitating performance was modeled at a moderate N_{ss} number of 20000 for 90 percent of design flow coefficient where rotational cavitation modes are present The source of this instability resulted from the interaction of the cavity with the neighboring blade leading to the detachment of the cavity that rotates relative to the blade and generates an asymmetric cavity pattern. The asymmetrical cavities generate a large radial load on the shaft which rotates at the fundamental mode of the rotational cavitation. For the sub-scale configuration the radial force amplitude was 186 lb-f which gives a non-dimensional force factor of 0.0116.

Spectral analyses of the dynamic pressure traces on the shroud, at the leading edge plane, were compared with experimental measurements. The fundamental rotational cavitation mode was observed to be 125 Hz which is approximately 1.29 N (rotational frequency is 96.6. Hz); both the frequency and relative amplitude compared well with the unsteady measurements. In addition to the fundamental rotation cavitation mode the data shows substantial energy with multiple peaks in the 5 -7.5 N range. This range was reasonably represented in the numerical results although the spectrum was not as rich. A helical pressure wave at the fundamental mode is found to propagate upstream and a potential for interaction with structural elements was identified.

INTRODUCTION

The primary parameter used in the design process to quantify cavitating performance of inducers is the critical suction specific speed, N_{ss}, at which head breakdown occurs. It is important to note that this parameter is a mean quantity assuming steady-state operation of the inducer and does not take dynamic pressure loads due to unsteady effects into account. However, since cavitation instabilities set in well before head breakdown occurs substantial unsteady pressure loads may result on blade surfaces particularly at off-design, low flow conditions. Furthermore, asymmetrical cavitation zones between blade passages generate large radial loads on the shaft. Hence, to account for these dynamic effects the effective operating margin of the inducer is reduced relative to the critical suction specific speed; this margin of safety increases the further off-design the flow rate is. Hence, the ability to predict the dynamic loads on the blades and the shaft though numerical simulations would be a valuable tool in helping quantify safe operating margins of inducer operation as well as understanding implications of design trade-offs.

The range of cavitation instabilities that can occur in an inducer is diverse and complex and can assume various forms as the inlet pressure is decreased (or N_{ss} number is increased). Typically, as the N_{ss} number is increased the cavity lengths on the blades get longer and eventually become unsteady leading

to rotation cavitation wherein the cavities detach from the blades and rotate relative to it generating a fluctuating load. The most common manifestation of rotational cavitation is an instability whose frequency is slightly higher than the rotational frequency. We note that various other rotational cavitation modes that can either rotate faster (up to 5 N) or slower have been reported by Tsujimoto and coworkers [1]. However, in either case the cavitation rotation modes are a local flow instability that are less sensitive to upstream or downstream effects from the system.

In contrast to the rotational cavitation modes, cavitation surge is a low frequency instability (1-6 Hz), that generates large amplitude axial disturbances that are in-phase azimuthally. This instability typically occurs at flow rates much lower than the design flow coefficient, where flow incidence to the blade gets large enough to cause separation at the inlet tip; the formation of an unstable, fluctuating vapor core upstream of the inducer generates low frequency periodic oscillations. These oscillations may couple with system dynamics to generate system wide instabilities.

Measurements of fluctuating blade stress on a three-bladed inducer similar to the inducer on the LE-7A liquid hydrogen turbopump are reported by Fujii et al [2]. Their results indicate that while the fluctuating stresses were large for all cavitation instability regimes, the amplitude was the highest when the instability was transitioning from a rotational cavitation mode to a surge mode. The authors labeled this mode as M.A.C. or "movement of asymmetric cavitation"; fluctuating stress levels here were well above 100 percent of the mean stress levels measured. The large amplitude of *these fluctuating stress levels* was believed to be the cause of shaft vibration in hot fire tests of LE-7A engine leading to unsafe operation. We note that currently the ability to predict dynamic cavitation loads with CFD tools is not mature and in general there is a dearth of detailed experimental data as well that may be used to both better understand the physics and validate the CFD tools.

There has been extensive work on developing analytical procedures to quantify instability behavior of cavitating pumps (Brennen and Acosta [3], Ng and Brennen [4], Tsujimoto et al. [5]). These procedures have developed techniques for defining a transfer matrix that characterizes the relationship between the fluctuating pressure and mass flow at the inlet with the same quantities at the discharge. Two important parameters influencing the transfer matrix were identified; a cavitation compliance factor (compressibility of flow), and a mass flow gain factor (cavity volume response to pressure fluctuations). While the dynamical transfer function technique has been used extensively to study unsteady behavior of inducers, one of the difficulties faced is the accurate specification of the compliance and mass flow gain factors. Brennen and Acosta [3] developed procedures to analytically define these coefficients using free streamline solutions on fully cavitating cascades. However this analysis is applicable to low frequency modes since it is essentially a quasi-static analysis. Experimental data on dynamical behavior of the low pressure oxidizer turbopump of the SSME was obtained by Ng and Brennen [4] where the transfer matrix was deduced directly from measurements. While these analytical tools are extremely valuable, defining

the appropriate matrix for an inducer configuration is challenging and requires experimental data for calibration.

As our discussion above indicates, there is a clear need for CFD tools that can predict the dynamical behavior of cavitating inducers particularly at off-design conditions. However, due to the lack of rigorous unsteady cavitation models and boundary conditions, as well as the general complexity of the problem, CFD technology is currently limited to simulating mean cavitating performance (i.e. head drop) at design conditions in water (Athavale and Singhal [6], Dupont and Okamura [7], Medvitz et al. [8], Hosangadi et al. [9]). The ability to model thermal effects and their impact on the *mean* performance of cryogenic inducers with thermal represents the current state-of-the-art (Hosangadi et al. [10],[11] , Dorney [12]). Unsteady 3-D numerical simulations, to obtain rotational cavitational modes in pumps have not been attempted by any group to the best of our knowledge; most studies in the literature are 2-D unsteady CFD simulations for cloud cavitation over isolated airfoils (Song et al. [13]) or stationary cascades (Iga et al. [14], Coutier-Delgosha et al. [15]).

The work presented here is the first to demonstrate the ability to numerically simulate cavitation instabilities within three-dimensional inducer configurations. It builds upon a numerical framework CRUNCH CFD® that has been extensively validated for cavitation in cryogenic fluids with thermal effects (Hosangadi and Ahuja [10]). Our focus here is on rotational cavitation modes at moderate Nss numbers where detailed comparisons have been made with experimental data taken at NASA MSFC (Skelley [16], Mulder [17]) for the sub-scale SSME low-pressure fuel pump (LPFP). The numerical simulations presented here modeled the experimental configuration closely and extensive comparisons of the simulations with the experimental data were conducted. Prior to performing unsteady cavitating simulations, the swirling back-flow upstream of the inducer was validated by comparing the calculations with the experimentally measured velocity profiles for off-design, low-flow conditions down to 70 percent of the design flow. Unsteady simulations of rotational cavitation were carried out at 90 percent of the design flow rate. Detailed comparison of the dynamic pressure loads and frequency of pressure fluctuations near the shroud were made with the experimental measurements. In addition, the resulting radial force and its frequency were tracked to estimate the resulting dynamic loads on the shaft.

MULTI-PHASE EQUATION SYSTEM

We give a very brief overview of the basic multiphase equation system here and refer the reader to Hosangadi and Ahuja [10] for more details. The equation system is written solved in a pressure based form as:

$$\Gamma \frac{\partial Q_v}{\partial t} + \frac{\partial E}{\partial x} + \frac{\partial F}{\partial y} + \frac{\partial G}{\partial z} = S + D_v \tag{1}$$

$$Q_v = \begin{pmatrix} P \\ u \\ v \\ w \\ \phi_g \\ h_m \\ k \\ \varepsilon \end{pmatrix} \qquad E = \begin{pmatrix} \rho_m u \\ \rho_m u^2 + P \\ \rho_m uv \\ \rho_m uw \\ \rho_g \phi_g u \\ \rho_m h_m u \\ \rho_m k u \\ \rho_m \varepsilon u \end{pmatrix} \qquad S = \begin{pmatrix} 0 \\ 0 \\ 0 \\ 0 \\ m_t \\ m_t h_{fg} \\ S_k \\ S_\varepsilon \end{pmatrix} \qquad (2)$$

The vectors Qv, E and S are given above. The matrix $\Gamma (= \partial Q / \partial Q_v)$ defines the transformation from the conservative to primitive variables and may further be preconditioned to obtain an efficient time-marching scheme (we refer the reader to Ref. [10] for more details).

The source term for the vapor phase arises due to cavitation where m_t is the net rate of vapor mass generation (or condensation), and the corresponding source term for the energy equation is given as $m_t h_{fg}$ where h_{fg} is the change in enthalpy resulting from the phase change and is a function of the local fluid temperature. These phase change source terms are discussed in a later section.

The mixture density, enthalpy, and vapor volume fraction are related by the following relations locally in a given cell volume:

$$\rho_m = \rho_g \phi_g + \rho_L \phi_L \qquad (3)$$

$$\rho_m h_m = \rho_g \phi_g h_g + \rho_L \phi_L h_L \qquad (4)$$

$$1 = \phi_g + \phi_L \qquad (5)$$

where ρ_g, ρ_L are the physical material densities, while h_g and h_L are the sensible enthalpy of the vapor and liquid phase respectively, and in general are functions of both the local temperature and pressure. In our study here, these properties were generated from the Standard thermodynamic database 12 available from NIST for pure fluids [18]. The thermodynamic properties of the fluid where specified using the saturation values from the table corresponding to the local temperature of the fluid. Equations (1)-(2) represent a stiff system with large variations in the acoustic speed that are a function of the local multi-phase composition. Preconditioning techniques are used to overcome this stiffness and obtain an efficient numerical scheme [10].

CAVITATION SOURCE TERMS

In the present effort, the cavitation source term is defined via a simplified non-equilibrium, finite rate form as follows:

$$m_t = K_f \rho_L \phi_L + K_b \rho_g \phi_g \qquad (6)$$

where the constant K_f is the rate constant for vapor being generated from liquid in a region where the local pressure is less than the vapor pressure. Conversely, K_b is the rate constant for reconversion of vapor back to liquid in regions where the

pressure exceeds the vapor pressure. Here, the rate constants are specified using the form given by Merkle [19].

$$K_b = \left| \begin{array}{ll} 0 & p < p_v \\ \dfrac{1}{\tau_b}\left(\dfrac{Q_\infty}{L_\infty}\right) & [\dfrac{p - p_v}{\frac{1}{2}\rho_\infty Q_\infty^2}] \quad p > p_v \end{array} \right|$$

$$K_f = \left| \begin{array}{ll} 0 & p > p_v \\ \dfrac{1}{\tau_f}\left(\dfrac{Q_\infty}{L_\infty}\right) & [\dfrac{p - p_v}{\frac{1}{2}\rho_\infty Q_\infty^2}] \quad p < p_v \end{array} \right|$$

$$p_v = p_\infty - \frac{1}{2}\rho_\infty Q_\infty^2 * CavNo.$$

$$\tau_f = \text{Time constant for vapor formation}$$

$$\tau_b = \text{Time constant for liquid reconversion} \qquad (7)$$

$$Cav.No. = \frac{p_\infty - p_v}{\frac{1}{2}\rho_\infty Q_\infty^2}$$

We note that for steady attached cavitation this simplified form may be adequate here since we are modeling interactions between the cavity and the neighboring blades. Higher frequency phenomenal such as clouds collapse is not the focus here.

SSME LOW PRESSURE FUEL PUMP SIMUATIONS

The SSME low -pressure fuel pump configuration that has been modeled is shown in Figure 1; it has four main blades and four splitter blades with a tip diameter of 6.044 inches and an axial length of 2.697 inches corresponding to a 0.5031 scaled configuration. The sub-scale geometry tested has a constant tip radius while the flight geometry has a slight increase in the tip radius from leading to trailing edge. The tip gap specified in the calculations was 0.014 inches which is in the range of tip gap estimates in the experimental configuration. Simulations were conducted at a rotational speed of 5800 rpm which simulates one of the test series conducted (Skelley [16]). A multi-element unstructured grid was generated using GRIDGEN where hexahedral blocks between blades connected with unstructured blocks to avoid skewness between blades; the total grid size was on the order of 5 million cells. The inlet boundary location varied depending on the flow coefficient to account for the larger back-flow extent as the flow coefficient drops; for 90 percent of design flow rate the inlet boundary was approximately 21 inches upstream, while for the 70 percent of design flow rate the boundary was approximately 35 inches upstream of the inducer.

Boundary conditions that were enforced are as follows: subsonic inflow conditions with enforced mass flux were specified at the inlet while a constant back pressure with a radial variation to satisfy equilibrium conditions corresponding to the swirl velocity at the exit. These conditions would need to be upgraded for cavitation surge problem where axial instabilities lead to large fluctuations in the mass flow that can couple to system dynamics and is an area we are currently working on. However for the rotational cavitation problem, where the instability is a local phenomena these conditions were deemed adequate. The simulations presented in this paper have been computed within an unsteady RANS framework

using a two equation k-ε model (see Ref. [20] for details). The decision to employ an unsteady RANS, as opposed to an LES framework, was based on the sensitivity of the back flow emanating from the inducer leading edge to the turbulence levels generated in the vortex upstream of the inducer; the grid resolution required for a LES calculation of the back flow (which extends for a substantial distance upstream), as well as high resolution of the fluctuating cavities on the blades would have been prohibitively expensive. A sensitivity of the reentrant jet to grid resolution within an LES calculation is shown in Ref. [16]. One consequence of using an unsteady RANS approach is that high frequency cavitation noise emanating from the cavity closure region is not possible. However as we shall discuss later the primary rotational cavitation modes are of the order of the rotational frequency of the pump and well within the resolution capable within an unsteady RANS framework.
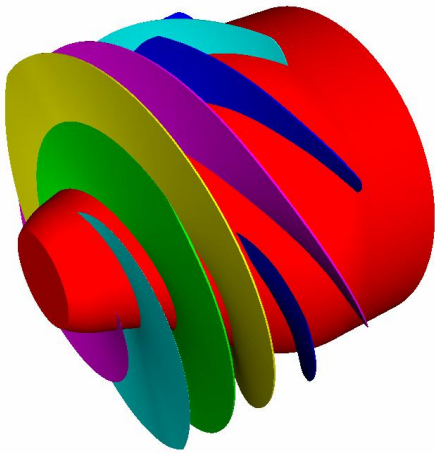
Figure 1. Geometry of Sub-Scale SSME Inducer Modeled.

Single Phase Flowfield Validation

Prior to performing cavitating simulations, the swirling back-flow upstream of the inducer inlet for off-design conditions was characterized and compared with experimental data for axial and swirl velocity measured at various upstream locations by Skelley [16]. We note that validating the back-flow is a critical step since the extent and magnitude of the swirl upstream directly influences the pressure drop in the core of the inlet. Two off-design flow coefficients were modeled; 90 percent of design (flow coefficient 0.0559) and 70 percent of design (flow coefficient 0.043). Figure 2 shows the meridional velocity and the tangential velocity for the 70 percent of design flow case (flow coefficient 0.043). A large swirling back-flow region is observed extending about 2 ½ diameters (18 inches) upstream of the leading edge. The swirl velocity region is consistent with the backflow region with peak swirl velocities about 9-10 times the inflow axial velocity. Figure 3 shows the pressure and turbulent viscosity contours. Large drop in the core pressure that is consistent with the swirling backflow is observed. Turbulence growth is large in the back-flow vortex where there is a large gradient in velocity demarcating the vortex region between the swirling back-flow and the non-swirling, inlet flow.
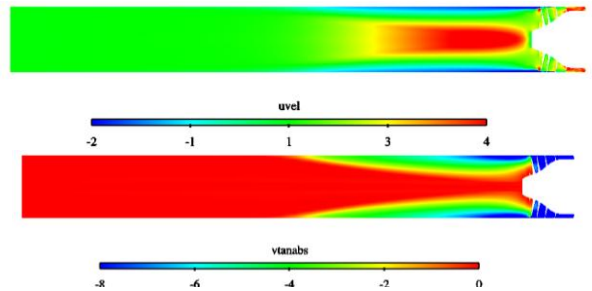

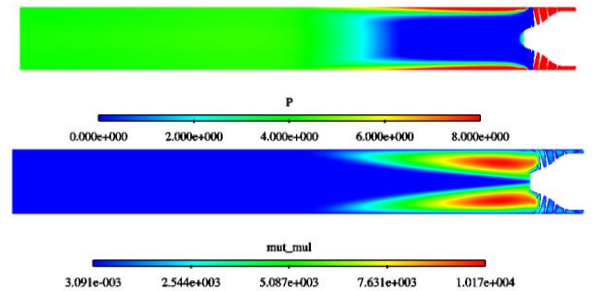**Figure 2. Meridional and Swirl Velocity Contours for 70% of Design Case.**

Figure 3. Pressure and Turbulent Viscosity Contours for 70% of Design Case.

Figure 4 shows the comparison of the swirl velocity for both the 70 percent of design, as well as at 90 percent of design flow rate, at three planes at which measurements were made: plane 700 (0.29 diameters), plane 500 (0.49 diameters), and plane 300 (0.99 diameters) upstream of the tip location. The solid lines are the experimental measurements while the dashed lines are the numerical calculations (the colors and symbols are kept consistent for each plane location). In general the predicted magnitude and extent of swirl is good overall at both flow coefficients. Both the shape and magnitude of the swirl velocity are predicted quite well (note that the values of swirl in the 70 percent case are much higher than in the 90 percent case). The corresponding axial velocity comparisons are shown in Figure 5. The comparison for the 90 percent case is excellent at all three planes. However, the axial velocity profiles for the 70 percent case while reasonable show some differences. In particular the axial velocity at plane 300 (which is a diameter upstream) shows a higher magnitude than the experimental value in the core while the comparisons at plane 500 and 700 (red and green curves) are much better.
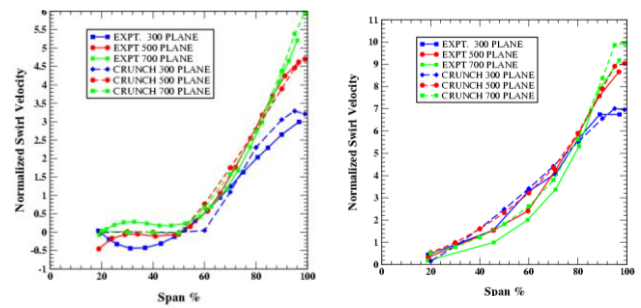
(a) 90% of Design
(b) 70% of Design

Figure 4. Comparisons of Swirl Velocity Profiles with Experimental Data from Skelley [16].
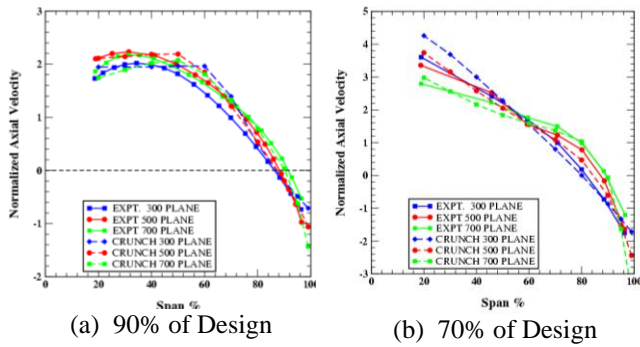
(a) 90% of Design   (b) 70% of Design

Figure 5. Comparisons of Axial Velocity Profiles with Experimental Data from Skelley [16].

Unsteady Cavitating Simulations

Cavitating calculations were conducted for a range of Nss numbers at a flow coefficient of 0.0559 (90 percent of the design flow rate). Large scale unsteadiness with asymmetric cavitation patterns was observed even at moderate cavitation numbers and subsequently we focused our attention on analyzing the cavitation instability at an Nss number of 20000 in detail.

Figure 6 shows the evolution of the rotational cavitation instability where the cavity detaches from the blade and seems to travel between blades. The time step between each plot in this sequence is 1/4th of a cycle for a rotational speed of 5800 rpm. We note that the plots shown here are in rotational frame so the plot shows the blades at a fixed location. Highly asymmetrical cavitation patterns are observed between blades; For instance at time snapshot 1, the blue blade has an extremely small cavity and the size of the cavity gets progressively larger as we go to the green blade and subsequently the red and purple blade. At time snapshot 2, the cavity on the green blade (which is the direction of the rotation) is getting smaller and by time snapshot 3 the cavity on the green blade has been completely wiped out! This same sequence of the blade getting "wetted' and the cavity being swept out continues to progress in sequence to the red blade (snapshot 6) and eventually to the purple blade (snapshot 9). By time snapshot 5, when one full cycle at 5800 rpm has been completed we find that the smallest cavity is not on the blue blade but has jumped to the green blade (which is one blade ahead in the direction of the rotation). This would imply that the pressure disturbance (which corresponds to the cavity getting cleaned and the blade becoming "wetted") is traveling at a frequency roughly 1.25 times the frequency of inducer rotation.

The sequence of the cavitation instability can also be visualized in a two-dimensional view by taking a cylindrical cut at a radius of 2.9 inches (close to the tip) and unrolling it as a planar surface. Figure 7 shows the cavity vapor contours on this cylindrical surface at the same times as the three-dimensional vapor isosurfaces shown in Figure 6; Note however the manner in which the cylinder is unrolled results in the direction of rotation pointing down for a counterclockwise direction. The asymmetry in the cavity sizes between the blades is now even more apparent with the cavity on one blade being very small and a variation of sizes on the neighboring blade, the corresponding pressure contours (Figure 8) plotted on a compressed scale of -3 to 3 psi (relative to the inlet pressure) shows a high pressure wave track the blade that gets "wetted" as the instability jumps from blade to blade with three low pressure regions corresponding to the blades that do have cavities on them.
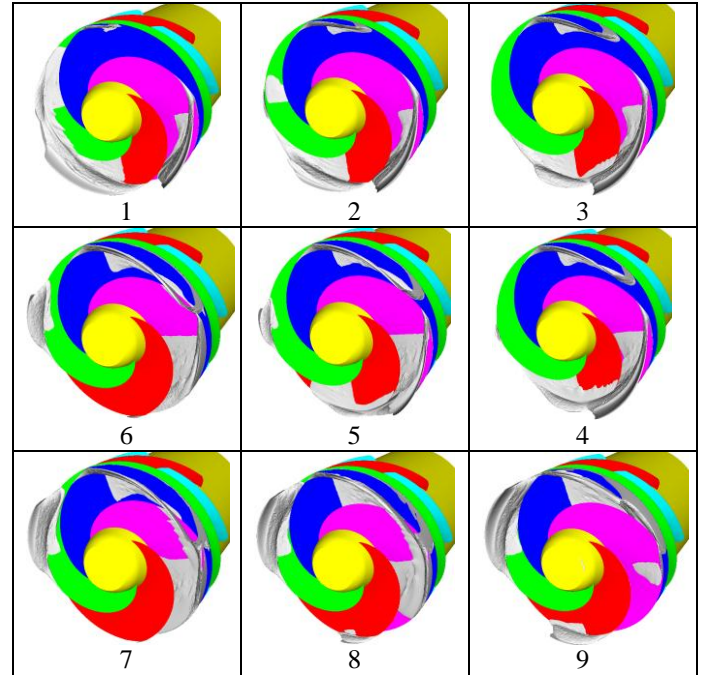

Figure 6. Unsteady Solution of Cavitating flowfield at N_{ss} of 20,000 for 90% of Design Case.
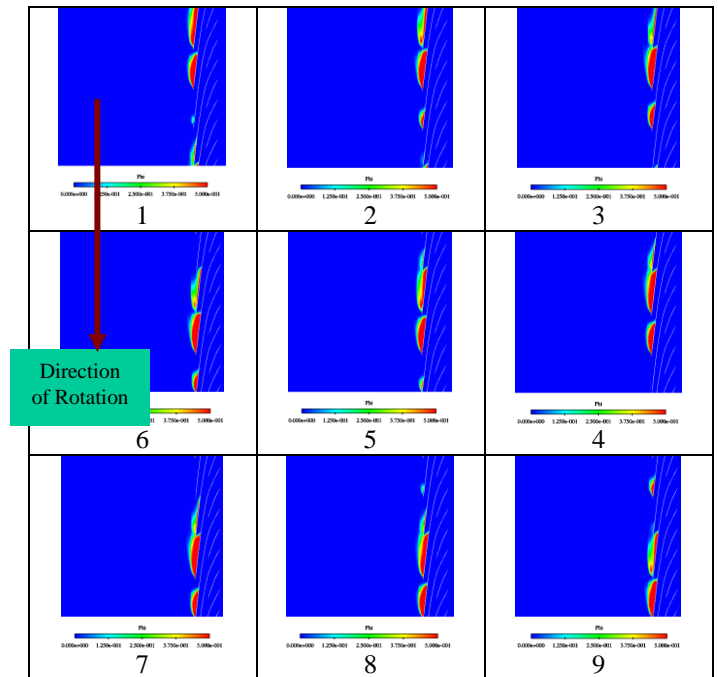

Figure 7. Vapor Contours on a Radial Cross Section at a Radius of 2.9 inches for N_{ss} = 20000.

The propagation of pressure waves upstream of the inducer due to the cavitation instability are illustrated via pressure contours on three axial planes (Figure 9) that are 0.5 inches, 4 inches, and 8 inches upstream of the inducer. At the plane

5

closest to the inducer (0.5 inches upstream), we see a very strong azimuthal variation in pressure. We note the following: 1) the low pressure regions are more prominent at the lower radii values possibly because of coupling with the backflow region while the high pressure region appears to correlate with the blade that is "wetted" and travels circumferentially around, 2) The pressure variations are substantial on the plane 4 inches upstream and are even noticeable on the farthest plane that is 8 inches upstream.
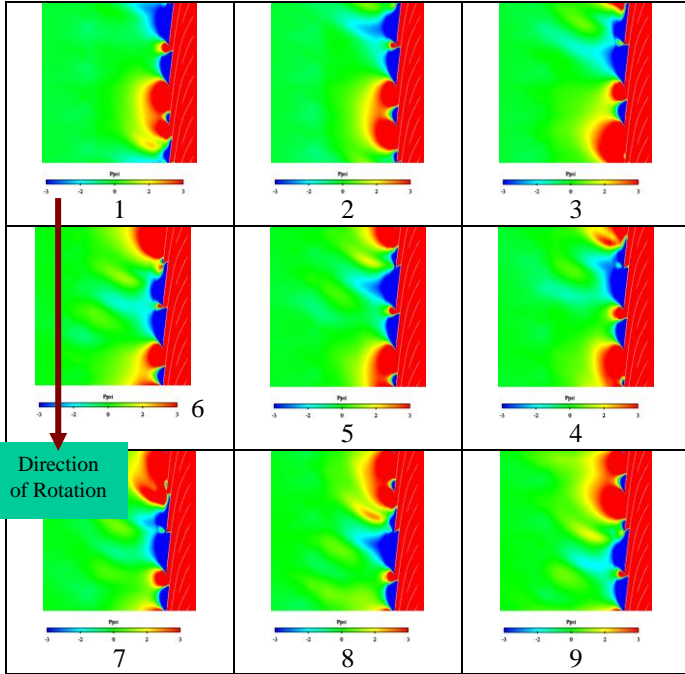
Figure 8. Pressure Contours on a Radial Cross-Section at a Radius of 2.9 inches for Nss = 2000.
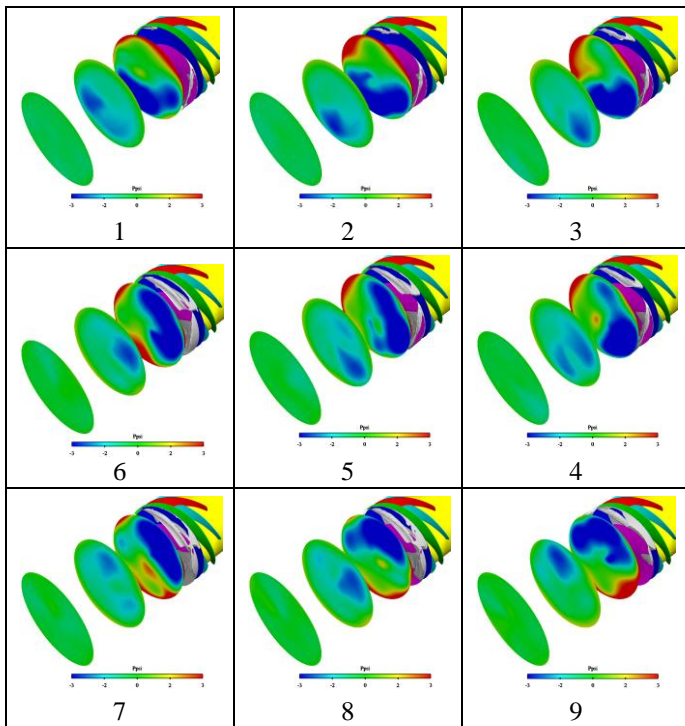

Figure 9. Pressure Contours on an Axial Cross Section for N$_{ss}$ = 20000 at X = 0.5, 4.0, 8.0 Inches Upstream Of Inducer.

Detailed quantitative analysis of pressure fluctuations and radial forces are presented. Figure 10 shows the pressure fluctuations on the shroud near the leading edge of the inducer (Plane 1000). Dynamic amplitudes of 100-200 percent of the mean pressures are observed. More importantly, a pattern of three pressure peaks is observed which corresponds to the passage of the blades with different cavity lengths passing by the probe during each rotational cycle; we observe that the blade number associated with the smallest peak is jumping to a consecutive blade after roughly each rotation.
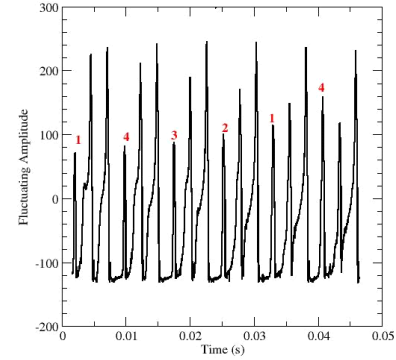

Figure 10. Cyclic Behavior of Pressure Trace at the Leading Edge Resulting from Rotational Cavitation.

Pressure traces attached to the rotating blades on the suction side at the leading edge are shown in Figure 11. The pressure traces on all four blades are plotted with the same color sequence as was shown in the unsteady contour sequence shown in Figure 11b. The large amplitude pressure spike on the suction side of the blade leading edge corresponds to the cavity being wiped clean from the blade. The sequence of the instability in the direction of blade rotation is as follows: the instability jumps from the green blade to the red, purple and blue blade in sequence before returning to the green blade after approximately four rotational cycles. The time period between the blade-to-blade cavity instability relative to blade rotational speed is 0.0087 s which corresponds to a 114 Hz frequency and is extremely periodic. Therefore, the frequency at which the cavity on the same blade is getting wiped out on the same blade is 28.5(or 114/4) Hz relative to blade rotational speed. However, since the blade itself is rotating at 96.6 Hz, the physical frequency in space fixed coordinates is 125.1 Hz which as we shall see later is the rotational cavitation mode observed on the probes at Plane 1000.
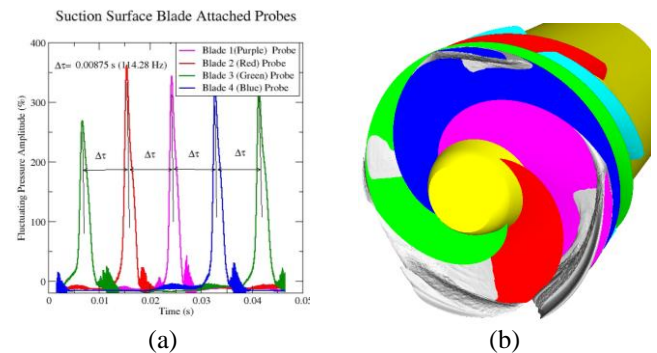

(a)   (b)

Figure 11. Pressure Trace on Suction Surface of Blade at Leading Edge (Plane 1000).

One of the interesting observations is that when the cavity gets wiped out from the suction side of the blade it simultaneously gets formed on the pressure side. Figure 12 shows the pressure (Figure 12a) and volume fraction (Figure 12b) plotted on the pressure (red color) and suction side (blue color) of one blade. Note that the colors here do not denote different blades but are only meant to distinguish the pressure and suction side of the same blade. Figure 12a clearly shows the jumping of the cavity from the suction side to the pressure side as the cavitation instability rotates and changes the incidence angle of the flow to the blade. Thus the pressure side has a high pressure for the majority of the time except for a short period when there is cavitation on it as the instability rotates; this flipping of the cavity from the suction to the pressure side occurs at a frequency of 28.5 Hz relative to blade rotation or at 125.1 Hz in an absolute frame. More importantly, from a structural integrity viewpoint, the bending moment at the leading edge tip changes sign over a duration of roughly 0.005 s (or half a rotation cycle) and this flipping of the bending moment occurs with a frequency of 125 Hz which is the rotational cavitation instability model.
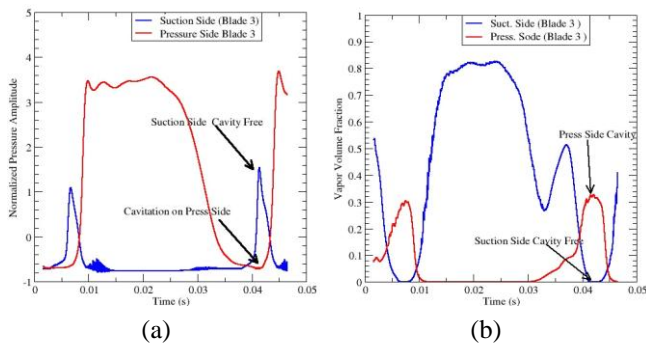

Figure 12. Interaction Between Pressure and Suction Side of Mode Due to Rotational Cavitation.

The rotational cavitation instability is observed to generate an oscillating radial force on the shaft. Figure 13 plots the phase of the radial force (shown in red) compared with the phase of the rotational frequency (shown in black). Not surprisingly the radial force is observed to have a frequency of 125 Hz that matches the rotational cavitation mode. The phase diagram of the force in y and z directions is plotted in Figure 14. The amplitude of the radial force is observed to be around 180 lb-f. Non-dimensionalizing this force by the tip dynamic head and the plan area of the inducer gives a radial force factor of 0.0116 which may then be used to scale the radial force to a full-scale configuration. Although the radial shaft force was not measured in these experiments, the non-dimensional force factor was deemed to be a realistic number based on experience with other inducers tested at NASA MSFC (Zoladz [21]). We note that the fluctuating radial force can generate an eccentricity in the shaft that can potentially lead to the blades scraping the shroud. The ability to predict the magnitude of radial forces on the shaft represents a significant advancement in the ability of CFD tools to support design and analysis of inducers since it is a difficult quantity to measure experimentally.
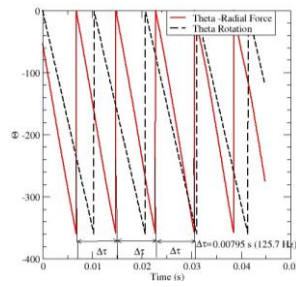

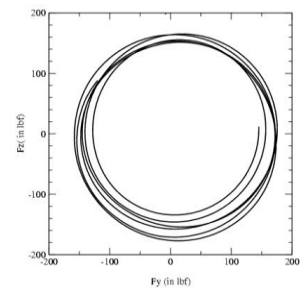Figure 13. Phase of the Rotating Radial Force on the Shaft.

Figure 14. Phase Diagram of Radial Force Components in Cartesian Coordinates.

An analysis of the spectral content and amplitude of the unsteady pressure fluctuations on the shroud is presented. In the computations there were 6000 steps per each rotational cycle (at 5800 rpm) giving a sampling rate of 1.724 micro-seconds. Calculations were performed over a total of approximately 4.3 rotational cycles; this gives a resolution of 22.3 Hz on the fft's using the numerical pressure traces reported here. In contrast, the experimental data was taken over 1933 rotational cycles (or 20 s) and therefore the resolution on the experimental data is significantly higher and can resolve the lower frequency modes better. However as we shall discuss below many of the dominant dynamic modes observed in the experimental traces were also evidenced in the numerical simulations.

The frequency content of the pressure fluctuations on the shroud at Plane 1000 (leading edge) are compared with the experimental frequency spectrum (taken by Mulder [17]) in Figure 15. The comparison is quite good with most of the major modes being duplicated. The largest amplitude is seen at the blade passage frequency of 386 Hz. However, the fundamental rotational cavitation mode of 125 Hz (Mode A) (which is around 1.29 N) and its overtone at 250 Hz (Mode B) also compare well. The only discrepancy seems to be that the experimental trace shows two closely spaced peaks for Mode A ; one at 122 Hz and another peak at 95 Hz. The resolution of the numerical fft trace as mentioned earlier is only 22 Hz and hence these two peaks cannot be independently resolved in the numerical trace where we instead get a broad peak. However the physical source of these two closely spaced peaks at Mode A (as well as Mode B) is not entirely clear. The experimental data shows multiple frequency peaks 500-750 Hz range. These peaks are surmised to arise from the high frequency cavitation noise that occurs as the cavity gets reestablished on a blade after the original cavity is wiped out during the rotational cavitation instability. The numerical traces also show two broad peaks (mode D and E) in this frequency range but the spectrum is not as rich as the experimental data. The modes F and G are overtones of the blade passage frequency and are captured in the numerical simulations as well.

The frequency content of the pressure fluctuations at various locations on the shroud are plotted in Figure 16 and compared to the spectrum at the leading edge (Plane 1000) location. The spectra at Plane 500 and Plane 700 show only the rotational cavitation mode (Mode A); thus as mentioned earlier

the source of almost all the dynamic fluctuations observed upstream appear to arise from the rotational cavitation instability. The spectrum at the downstream location shows a dominant mode at the blade passage frequency with a smaller peak at the fundamental cavitation mode of 125 Hz. At both the upstream and downstream location Mode B (260 Hz) as well as Mode D and E seem to be clamped substantially indicating that these modes are essentially local phenomena to the Plane 1000 location where the cavitation noise is the largest while only the fundamental instability mode of 125 Hz permeates the entire inducer flowfield both upstream and downstream of the leading edge.
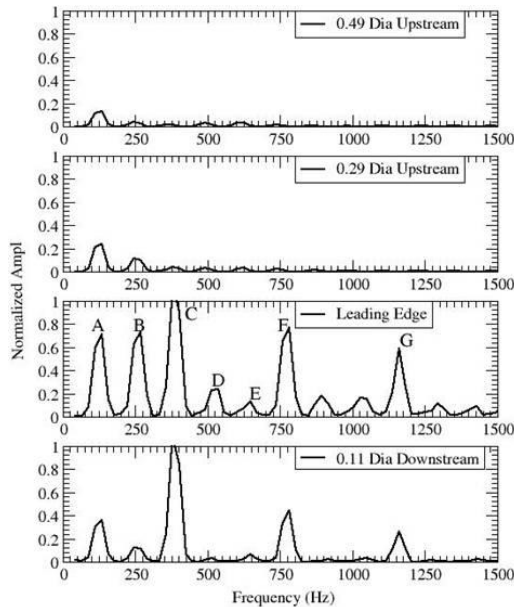

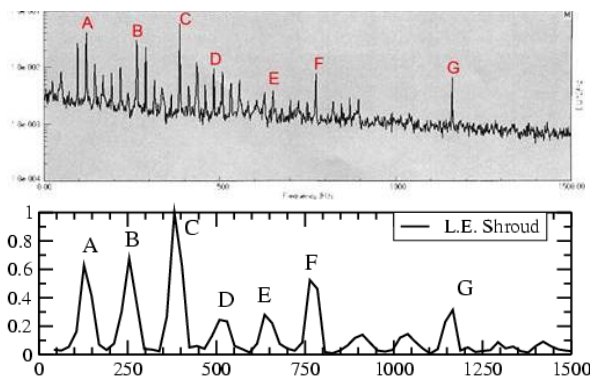**Figure 15. Frequency Spectra of Pressure Fluctuations at Various Locations on the Shroud.**

Figure 16. Comparison of Frequency Content at the Leading Edge on the Shroud with Experimental Data from Mulder [17].

CONCLUSION

Detailed simulations of a sub-scale configuration of the SSME low pressure fuel pump at off-design conditions have been conducted and compared with experimental data taken at NASA MSFC (Skelley [16], Mulder [17]). The swirling back flow resulting from the increased incidence angle of the flow to the blade was validated for non-cavitating flows by comparing

swirl and axial velocity profiles for flow rates of 90 and 70 percent of the design flow coefficient. Good comparison for the swirl profiles at both flow coefficients, while the axial velocity profile comparison was reasonable at the low flow coefficient of 70 percent of design. The low pressure in the inlet core due to the back-flow vortex was quantified in the numerical simulations.

Unsteady cavitating simulations at a moderate N_{ss} number of 20000 were conducted for the 90 percent of design flow coefficient and rotational cavitation modes were observed to set in. The source of this instability was the interaction of the cavity with the neighboring blade that results in the flow incidence being altered at the neighboring blade and leading to the detachment of the cavity. The detached vapor rotates relative to the blade leading to asymmetrical cavitation patterns that vary periodically at a rate given by the difference between the instability frequency and the rotational frequency of the pump. The instability also results in a cavity forming on the pressure side of the blade, and a reversal in blade loading, over finite time periods as the cavity moves relative to the blade.

The asymmetrical cavities between the blade passageways results in a large radial load on the shaft. The radial load amplitude in the subscale configuration was 186 lb-f which gives a force factor of 0.0116 when non-dimensionalized by the tip dynamic head and the planar area of the inducer. Furthermore the radial force on the shaft was observed to be rotating at the fundamental mode of the rotational cavitation. The non-dimensional force factor may be used to estimate the shaft forces on the full-scale configuration and is an extremely useful measure to determine operational safety.

Spectral analyses of the dynamic pressure traces on the shroud near the leading edge plane were compared with experimental measurements at the same location. The fundamental rotational cavitation mode was observed to be 125 Hz which is approximately 1.29 N (rotational frequency is 96.6 Hz) and good comparison of the amplitude was obtained both for the fundamental mode as well as its first overtone. In addition to the fundamental rotation cavitation mode the experimental data shows substantial energy with multiple peaks in the 5 -7.5 N range (i.e. 500 -750 Hz). The numerical results also show two broad peaks in this range although the spectrum is not as rich. Analyses of the pressure spectrum at other locations on the inducer indicate that a helical pressure wave at the fundamental rotational cavitation mode travels upstream. The spectrum downstream of the leading edge shows energy in the fundamental rotational cavitation mode and the blade passage frequency. The energy in the high-frequency mode (5-7.5 N) appears to be damped.

NOMENCLATURE

A = amplitude of oscillation
A = cylinder diameter
C_p = pressure coefficient
Cx = force coefficient in the x direction
Cy = force coefficient in the y direction
C = chord
J = waypoint index
K = trailing-edge (TE) nondimensional angular deflection rate

REFERENCES

[1] Tsujimoto, Y., Yoshida, Y., Maekawa, Y., and Watanabe, S., Hashimoto, T., "Observations of Oscillating Cavitation of an Inducer," *ASME J. Fluids Eng*., Vol. 117, No. 4, pp. 775-781, 1997.

[2] Fujii, A., Azuma, S., Uchiumi, M, Yoshida, Y., and Tsujimoto, Y., "Unsteady Behavior of Asymmetric Cavitation in a 3-Blended Inducer," Fifth International Symposium on Caviation (Cav 2003), Osaka, Japan, Nov. 1-4, 2003.

[3] Brennen, C., and Acosta, A.J., (1976) "The Dynamic Transfer function for a Cavitating Inducer," *J. of Fluids Engineering*, Transactions of the ASME, V. 98, pp. 182-192.

[4] Ng, S.L. and Brennen, C., (1978) "Experiments on the Dynamic Behavior of Cavitating Pumps," *J. of Fluids Engineering*, Transactions of the ASME, V100, pp. 182-192.

[5] Tsujimoto, Y.,Kamyo, K and Brennen, C.F. "Unified Treatment of Flow Instabilities of Turbomachines," AIAA-99-2678, 35th AIAA/ASME/ SAE/ASEE Joint Propulsion Conference and Exhibit, Los Angeles, CA, June, 1999.

[6] Athavale, M.M., and Singhal, A.K., "Numerical Analysis of Cavitating Flows in Rocket Turbopump Elements", 37th AIAA Joint Propulsion Conference, July 2001.

[7] Dupont, P., and Okamura, T., "Cavitating Flow Calculations in Industry", The 9th International Symposium on Transport Phenomena and Dynamics of Rotating Turbomachinery, Honolulu, Hawaii, 2002.

[8] Medvitz, R.B., Kunz, R.F., Boger, D.A., Lindau, J.W., Yocum, A.M., Pauley, L.L., "Performance Analysis of Cavitating Flow in Centrifugal Pumps Using Multi-Phase CFD", *Journal Fluids Engg*., Vol. 124, pp. 377-383, 2002.

[9] Hosangadi, A., Ahuja, V., and Ungewitter, R.J. "Simulations Of Cavitating Flows In Turbopumps," *Journal of Propulsion and Power,* Vol. 20, No. 4, pp. 604-611, July-August, 2004.

[10] Hosangadi, A. and Ahuja, V., "Numerical Study Of Cavitation In Cryogenic Fluids," *Journal of Fluids Engineering*, Vol. 127, pp. 267-281, March 2005.

[11] Hosangadi, A., Ahuja, V., and Ungewitter, R.J., "Numerical Study Of A Flat Plate Inducer: Comparison Of Performance In Liquid Hydrogen And Water," AIAA-2006-5070, 42nd AIAA/ASME/SAE/ASEE Joint Propulsion Conference & Exhibit, 9 - 12 Jul 2006, Sacramento, CA.

[12] Dorney, D., L. Griffin, Marcu, B., and Williams, M., "Unsteady Flow Interactions Between the LH2 Feed Line and SSME LPFP Inducer**,"** AIAA-2006-5073, 42nd AIAA/ASME/SAE/ASEE JPC & Exhibit, 9 - 12 Jul 2006, Sacramento, CA.

[13] Song, C.S.S., and Qin, Q., (2001) "Numerical Simulations of Unsteady Cavitating Flows", *Proceedings of the Fourth International Symposium on Cavitation*, Pasadena.

[14] Iga, Y., Nohmi, M., Goto, A., Shin, B.R., and Ikohagi, T., "Numerical Analysis of Unstable Phenomena of Cavitation In Cascade With Finite Blade Numbers," The 9th International Symposium on Transport Phenomena and Dynamics of Rotating Turbomachinery, Honolulu, Hawaii, 2002.

[15] Coutier-Delgosha, O., Fortes-Patella, R., Reboud, J.L., (2003) "Evaluation of the Turbulence Model Influence on the Numerical Simulations of Unsteady Cavitation". J. Fluids Engg., Vol. 125 (No.1), pp.38-45.

[16] Skelley, S., (2005) "Space Shuttle Main Engine Low Pressure Fuel Pump Water Flow Test Report, Test P2397", Test P2397, NASA Marshall Space Flight Center, January, 2005.

[17] Mulder, A, (2005) "Space Shuttle Main Engine Low Pressure Fuel Pump Water Flow Test Report, Test P2397: Unsteady Data Characterization", Test P2397, NASA Marshall Space Flight Center, February 2005.

[18] Lemmon, E.W., McLinden, M.O., and Friend, D.G., "Thermophysical Properties of Fluid Systems" In NIST Chemistry WebBook, NIST Standard Reference Database Number 69, Eds. P.J. Linstrom and W.G. Mallard, June 2005, National Institute of Standards and Technology, Gaithersburg MD, 20899 (http://webbook.nist.gov).

[19] Merkle, C.L., Feng, J.Z. and Buelow, P.E.O., "Computational Modeling of the Dynamics of Sheet Cavitation," *Proceedings of the 3rd International Symposium on Cavitation*, Grenoble, 1998.

[20] Hosangadi, A., and Ahuja, V., "A Numerical Study of Cavitation in Cryogenic Fluids Part II: New Unsteady Model for Dense Cloud Cavitation," Paper No. 81, International Symposium on Cavitation, CAV2006, Wageningen, The Netherlands, 11-15 Sept. 2006.

[21] Zoladz, T. Personal Communication, NASA Marshall Space Flight Center, March 2005.